npj | quantum materials

Article

Published in partnership with Nanjing University

https://doi.org/10.1038/s41535-024-00647-1

Atomic-scale magnetic doping of monolayer stanene by revealing Kondo effect from self-assembled Fe spin entities

Nitin Kumar [1], Ye-Shun Lan[1], Iksu Jang[1,2], Yen-Hui Lin[1], Chia-Ju Chen[1], Tzu-Hsuan Lin[1], Horng-Tay Jeng [1,3,4,5] ✉, Po-Yao Chang [1] ✉ & Pin-Jui Hsu [1,3] ✉

Atomic-scale spin entity in a two-dimensional topological insulator lays the foundation to manufacture magnetic topological materials with single atomic thickness. Here, we have successfully fabricated Fe monomer, dimer and trimer doped in the monolayer stanene/Cu(111) through a low-temperature growth and systematically investigated Kondo effect by combining scanning tunneling microscopy/spectroscopy (STM/STS) with density functional theory (DFT) and numerical renormalization group (NRG) method. Given high spatial and energy resolution, tunneling conductance (d*I*/d*U*) spectra have resolved zero-bias Kondo resonance and resultant magnetic-field-dependent Zeeman splitting, yielding an effective spin $S_{eff} = 3/2$ with an easy-plane magnetic anisotropy on the self-assembled Fe atomic dopants. Reduced Kondo temperature along with attenuated Kondo intensity from Fe monomer to trimer have been further identified as a manifestation of Ruderman-Kittel-Kasuya-Yosida (RKKY) interaction between Sn-separated Fe atoms. Such magnetic Fe atom assembly in turn constitutes important cornerstones for tailoring topological band structures and developing magnetic phase transition in the single-atom-layer stanene.

In the low-temperature limit, Kondo effect originates from the collective interaction between an atomic spin entity and surrounding conduction electrons of non-magnetic metal[1–5]. In the strong coupling regime, localized atomic spin is antiferromagnetically (AFM) coupled, i.e., spin-spin exchange interaction $J < 0$, with the itinerant spin bath from conduction-band electrons of host metal. Below the characteristic Kondo temperature (T_K), such atomic spin is then effectively screened by the conduction electron spin cloud, resulting in the formation of a spin singlet ground state at the Fermi level (E_F)[6]. Besides an increase of electrical resistivity, a pronounced electronic resonance at E_F represents the distinctive hallmark of this highly-correlated many-body state, commonly referred to as the Kondo or Abrikosov–Suhl resonance[7–9]. In particular, zero-bias anomaly as a manifestation of Kondo resonance in the tunneling conductance (d*I*/d*U*) spectra can be accessed by utilizing scanning tunneling spectroscopy (STS)[8,10–15], offering an ideal approach not only to resolve individual Kondo adsorbates at the atomic scale, but also to explore magnetic field and temperature dependence of Kondo effect with a high energy resolution.

Stanene, a two-dimensional (2D) honeycomb lattice composed of Sn atoms, i.e., tin (Sn) analogue of graphene, has received extensive attention because of its intriguing topological properties. For example, nontrivial band topology from in-plane *s-p* band inversion and the emergence of topological edge states have been investigated by Deng et al. in the epitaxial growth of ultraflat monolayer (ML) stanene[16]. Owing to a large atomic mass of Sn, a prominent spin-orbit-coupling (SOC) gap opening up to about 0.3 eV has been uncovered from angle-resolved photoemission spectroscopy (ARPES) studies[16–18], contributing a key ingredient to fulfill quantum spin Hall effect (QSHE) and topological phase transition at room temperature (RT)[19–22]. Recently, introducing magnetism to 2D topological insulators arises as a spotlight issue in the pursuit of magnetic topological insulators (MTIs)[23–30]

[1]Department of Physics, National Tsing Hua University, Hsinchu 300044, Taiwan. [2] Institut für Theorie der Kondensierten Materie, Karlsruher Institut für Technologie, Karlsruhe 76049, Germany. [3]Center for Quantum Technology, National Tsing Hua University, Hsinchu 300044, Taiwan. [4]Physics Division, National Center for Theoretical Sciences, Taipei 10617, Taiwan. [5]Institute of Physics, Academia Sinica, Taipei 11529, Taiwan. ✉e-mail: jeng@phys.nthu.edu.tw; pychang@phys.nthu.edu.tw; pinjuihsu@phys.nthu.edu.tw

with reduced dimensionality, which exhibit quantum anomalous Hall effect (QAHE) and extraordinary quantum electronic transport without a need of applying external magnetic field[19,20,31]. Despite several exceptional aspects supporting stanene for a promising candidate of 2D topological insulator, research efforts relevant to the development of low-dimensional magnetic topological materials by incorporating magnetic ingredients, e.g., considerable magnetic moment and effective magnetic anisotropy, to single-atomic-layer stanene are still lacking and have not been reported yet.

In this work, we have carried out systematic studies on the Kondo effect of magnetic Fe atom assembly on stanene/Cu(111) by using low-temperature STM/STS together with theoretical DFT and NRG calculations. By depositing Fe atoms onto the stanene monolayer at 80 K, thermally energetic Fe atoms are able to replace Sn atoms and spontaneously arrange into monomer, dimer and trimer structures. The zero-bias Kondo resonance in the dI/dU spectra as well as corresponding Zeeman splitting under external magnetic field have been resolved, where an effective spin $S_{eff} = 3/2$ with an easy-plane magnetic anisotropy has been further characterized on the self-assembled Fe atomic dopants. Besides, Kondo temperature and Kondo peak amplitude continuously decreasing from Fe monomer to trimer are also conceivable from numerically simulated NRG results by taking substantial RKKY coupling between Sn-separated Fe atoms into account. After achieving the atomic-scale Fe doping and revealing the Kondo physics, one might have an opportunity to engineer topological band features and establish RKKY-induced magnetism in the magnetically-doped stanene monolayer.

Results and discussion

Growth of magnetic Fe atom Assembly/Stanene/Cu(111)

Figure 1a represents a topographic STM overview of as-grown Fe/stanene/Cu(111) sample prepared at 80 K, in which well-extended 2D stanene islands with an apparent height about 1.8 Å covering about two-thirds of Cu(111) surface can be observed. The enlargement from the white square frame in Fig. 1a has been shown in Fig. 1b, many small and bright protrusions resulting from deposited Fe atoms have been recognized on the surface of stanene/Cu(111). Figure 1c displays the atomically-resolved image of the white square frame from Fig. 1b, honeycomb-structured stanene has a (2×2) supercell, leading to a lattice constant of about 5.1 Å with respect to the (1×1) primitive unit cell of Cu(111)[16,32]. Interestingly, deposited Fe atoms have spontaneously arranged into three types of atomic structures, including monomer, dimer and trimer, as circled by green, yellow and blue colors, respectively, in Fig. 1c. Note that such self-assembled Fe atomic dopants on stanene/Cu(111) bear a close resemblance to the Co counterpart on stanene/Cu(111) as reported recently (see Supplementary Figs. 1–5 for details)[32]. A perspective view of schematic atomic model summarizing the Fe monomer, dimer and trimer on stanene/Cu(111) has been illustrated in Fig. 1d.

Monomer

Figure 2a is atomic-scale zoom-in of Fe monomer on stanene/Cu(111), where Fe atom appears as a bright protrusion in the center and surrounding Sn atoms in honeycomb lattice have a uniform atomic corrugation indicating the flatness of stanene monolayer. The Fe atom exhibits an apparent height about 12 pm in average, i.e., much lower than adsorbing single Fe atom directly on top of stanene, suggesting a possible substitution of one Sn atom by the highly energetic Fe atom from thermal e-beam evaporation. Figure 2b represents the resultant atomic structure obtained from self-consistent lattice relaxations in DFT, where Fe monomer is analogous to the surface doping of single Fe atom onto stanene[32]. Note that STM simulations have been further performed to crosscheck bias-dependent topographic images and line profiles with experimental observations (see Supplementary Fig. 2 for details).

A pronounced peak feature at E_F that could be attributed to the Kondo effect of Fe monomer has been resolved in the zero-magnetic-field dI/dU spectrum of the Fig. 2c (top curve), which is absent from the dI/dU spectra

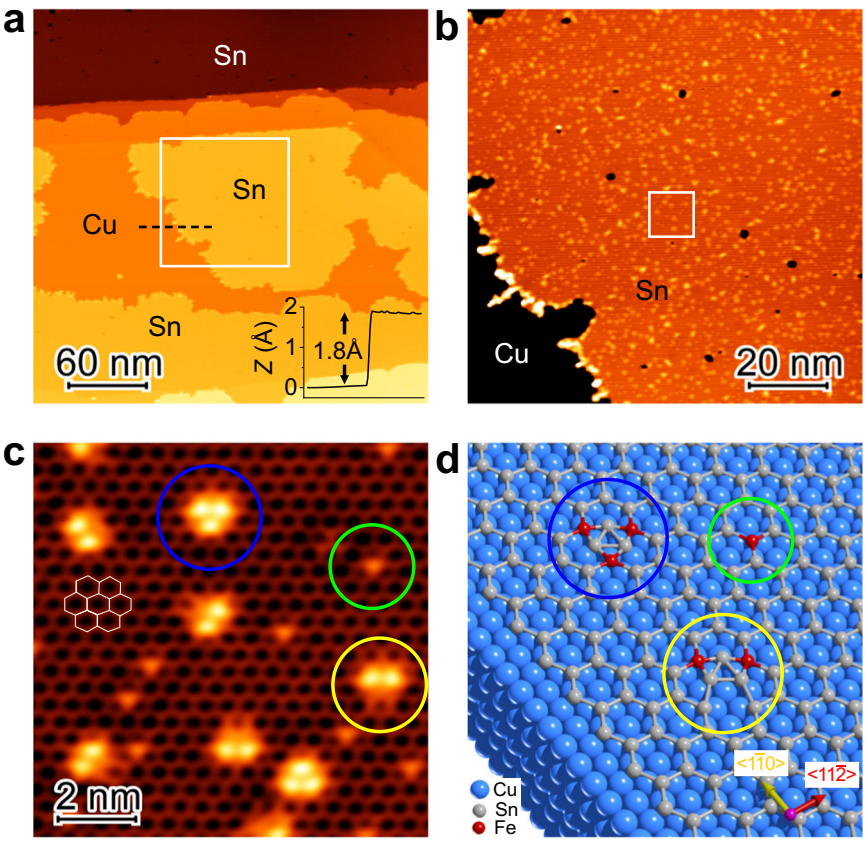

Fig. 1 | Fabrication of Fe atom assembly on monolayer stanene/Cu(111). a STM topographic overview of a dilute amount of Fe atoms deposited onto stanene/Cu(111) held at 80 K. The surface coverage of stanene is about 0.38 ML and a step height about 1.8 Å can be extracted on Cu(111) surface. **b** Zoom-in area marked by a white square frame in (**a**). The deposited Fe atoms can be seen as small bright protrusions atop the stanene. **c** Atomically resolved STM image acquired from the white square frame in (**b**), where the self-assembled Fe monomer, dimer and trimer are marked by green, yellow, and blue circles, respectively. **d** A perspective view of schematic atomic model summarizing the Fe monomer, dimer and trimer structures on stanene/Cu(111). (scanning parameters are $V_s = -1$ V and $I_t = 400$ pA for all topographic images).

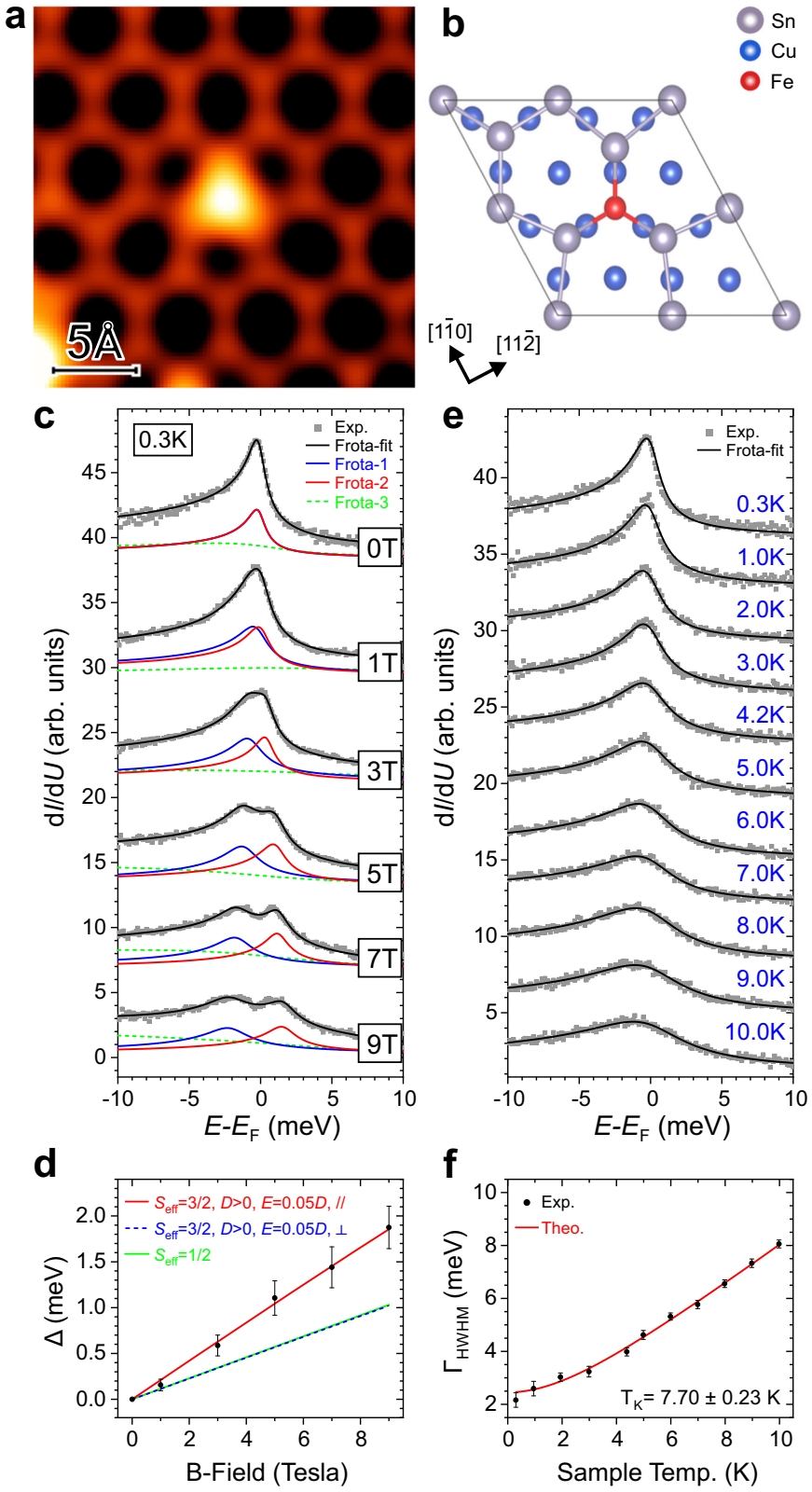

Fig. 2 | Field-dependent Kondo resonance and Kondo temperature measured from Fe monomer. **a** Atomically resolved STM topography of Fe monomer made from the substitution of one Sn atom on the honeycomb lattice of stanene/Cu(111). **b** Atomic Fe monomer structure fully relaxed from DFT calculations. **c** Magnetic field-dependent dI/dU spectra measured on the Fe monomer from 0 to 9 T fitted by the superposition of Frota functions. All spectra are vertically shifted for clear visibility. **d** Zeeman splittings of Kondo resonance fitted by effective spin Hamiltonian with magnetic anisotropy terms involved. **e** Temperature-dependent evolution of Kondo resonance from 0.3 to 10 K and corresponding Frota fits. **f** HWHM of Kondo resonance extracted from the Frota fits of (**e**) and $T_K = 7.70$ K can be determined by using Eq. (2). Error bars are defined by the standard deviation of fitting analyses. (stabilization parameters: $U_b = +10$ mV, $I_t = 1.0$ nA for all dI/dU curves).

acquired on stanene/Cu(111) and pristine Cu(111) substrate, respectively. The dI/dU spectra evolving with external magnetic fields applied normal to sample surface from 0 T to 9 T have been displayed in Fig. 2c, a clear splitting of the Kondo peak has been further revealed. Note that spin degeneracy of Kondo singlet state is lifted when an external magnetic field has been applied, resulting in the splitting of Kondo peak proportional to the strength of Zeeman energy[8,10–15]. It is also worth noting that zero-bias Kondo resonance was not observed even down to 0.3 K in the Co/stanene/Cu(111) due to a small magnetic moment of Co atom[32]. In addition to Cu(111) substrate, there are also energy bands around the Fermi level of single-atomic-layer

stanene, which should contribute to the conduction electron bath that screens out the Fe atomic spin.

To advance our understandings on the magnetic-field-dependent splitting of Kondo peak, experimental dI/dU spectra have been fitted to the Frota function[7,33,34]. We denote that both Frota and Fano fitting results are in line with each other (see Supplementary Fig. 6 for details), although Fano function may give a higher Kondo temperature[9]. In Fig. 2c, superposition of three Frota functions has been used to simulate the experimental data, Frota-1 and Frota-2 curves (blue and red lines) are referred to the Kondo resonances below and above the E_F, and Frota-3 curves (green dashed lines) are used to compensate the broad background. The consequent Zeeman energy ($\Delta(B)$), i.e., the half of Kondo peak splitting, has been extracted as black dots in Fig. 2d[8,10–15,35]. A linear fitting using the relation $\Delta(B) = g\mu_B B$ provides an unrealistically large value of $g = 3.64 \pm 0.10$, which excludes the simple assumption of $S_{eff} = 1/2$ case. To identify the spin state of Fe monomer, our experimental results have been further analyzed by effective spin Hamiltonian[12,36–39]:

$$\hat{\mathcal{H}}_{spin} = g\mu_B \hat{\vec{\mathbf{S}}}_{eff} \cdot \vec{\mathbf{B}} + D\hat{S}^2_{eff_z} + E(\hat{S}^2_{eff_x} - \hat{S}^2_{eff_y}) \quad (1)$$

where g is the Landé factor, μ_B is the Bohr magneton, $\hat{\vec{\mathbf{S}}}_{eff}$, $\hat{S}_{eff_x}$, $\hat{S}_{eff_y}$, and $\hat{S}_{eff_z}$ are the total effective spin operator and its projections on x, y, and z directions, D and E are the longitudinal and transverse magnetic anisotropies (see Supplementary Note). Since a single Kondo peak at zero bias in zero magnetic field can only be established by the first-order spin excitation in a degenerate ground state, where energy levels are connected by $\Delta m = \pm 1$, therefore neglecting the possibility of the integer S_{eff}. Moreover, for a negative longitudinal anisotropy ($D < 0$), energy levels with the highest $|m|$ of half-integer spins give rise to the ground state that no longer connects with $\Delta m = \pm 1$, restricting our analyses to $D > 0$, i.e., an easy-plane magnetic anisotropy. As the red solid line shown in Fig. 2d, our experimental data points (black dots) are fairly described by the Eq. (1) after diagonalizing Hamiltonian matrix, selecting correct spin sector and solving energy ground state, yielding a total effective spin $S_{eff} = 3/2$ with $g = 1.98 \pm 0.02$, $D = 3.13 \pm 0.24$ meV, and $E = 0.17 \pm 0.02$ meV. Because of atomic-scale orbital hybridization, bonding reconfiguration and charge density redistribution occurring in the substitution of Sn atoms[8,15,32], the Fe monomer has $S_{eff} = 3/2$ smaller than $S_{iso} = 4/2$ for the isolated Fe atom. Note that magnetic moment values ranged from 2.2 to 2.5 μ_B have been calculated for the Fe atom assembly/stanene/Cu(111) by DFT (see Supplementary Fig. 7 for details), supporting $S_{eff} = 3/2$ as extracted from Zeeman-split Kondo resonance experimentally. We would also like to denote that not only a reasonable g value and an easy-plane anisotropy ($D > 0$) with z-axis parallel to surface have been obtained, but also a very small E ($\approx 0.05D$), i.e., almost magnetically isotropic along transverse direction, has been characterized. On the other hand, the opposite outcome of z-axis normal to surface (blue dashed line) produces essentially the same behavior with the isotropic case of $S_{eff} = 1/2$ ($D = E = 0$) as the green solid line plotted in Fig. 2d[37–39].

Apart from magnetic-field-dependent splitting, temperature-dependent evolution of Kondo resonance from 0.3 K to 10 K has been shown in Fig. 2e. A Kondo temperature (T_K) of 7.70 ± 0.23 K has been determined by fitting the half-width at half-maximum (Γ_{HWHM}) as a function of sample temperature (black dots in Fig. 2f) with the following expression[14,15,37]:

$$\Gamma_{HWHM}(T) = 3.7\sqrt{(\alpha k_B T)^2 + (k_B T_K)^2} \quad (2)$$

where Γ_{HWHM} are extracted from the Frota fits of Fig. 2e (black curves) by using $\Gamma_{HWHM} = 2.542 \times \Gamma_{Frota}$, k_B is the Boltzmann constant, T is the sample temperature, T_K is Kondo temperature and α is a constant parameter. Note that the numerical prefactor of 3.7 is used to get the correct zero-temperature limit of $\Gamma_{HWHM}(0) = 3.7k_B T_K$, as described in the Wilson's definition of Kondo temperature[40] and NRG calculations[41].

Dimer

Unlike the Fe monomer, Fe dimer structure forms when two energetic Fe atoms jointly substitute two Sn atoms from stanene honeycomb lattice. As atomically resolved STM image shown in Fig. 3a, Fe dimer appears as a dumbbell-like protrusion in the center and exhibits an apparent height about 25 pm (see Supplementary Fig. 3 for details). The atomic structure model of Fe dimer fully relaxed from DFT has been shown in Fig. 3b, where neighboring Sn atoms are rearranged as a result of the local incorporation of heterogeneous Fe atoms. We would like to denote that several different structural models have been proposed for the Fe dimer, like previous studies on the Co dimer/stanene/Cu(111)[32], but they are not consistent with either experimental observations or theoretical calculations.

From the dI/dU spectrum measured on Fe dimer/stanene/Cu(111), zero-bias Kondo peak has also been observed (topmost, 0 T curve in Fig. 3c). The $\Delta(B)$ obtained from the fittings of Fig. 3c have been arranged into Fig. 3d. The best fit of experimental $\Delta(B)$ (black dots) has been successfully formulated by effective spin Hamiltonian in Eq. (1), providing $S_{eff} = 3/2$, $g = 2.01 \pm 0.02$, $D = 3.06 \pm 0.15$ meV, $E = 0.23 \pm 0.01$ meV, and z-axis parallel to the surface as the red line plotted in Fig. 3d. Temperature-dependent Kondo resonance has been shown in Fig. 3(e), where the Frota fitting analyses (black curves) reproduce the broadening of zero-bias peak in the dI/dU spectra (grey squares). Figure 3f summarizes the $\Gamma_{HWHM}(T)$, and the T_K value of 7.10 ± 0.28 K by fitting the Eq. (2) derived for the Fe dimer/stanene/Cu(111).

Trimer

Enlightened by the Fe dimer formation, thermally energetic Fe atoms would likely nucleate first on top of stanene, and then substitute the Sn atoms to develop the Fe trimer structure[32]. An upside-down triangle composed of three Fe atoms, i.e., bright dot-like protrusions, for the Fe trimer on stanene/Cu(111) has been atomically resolved in the Fig. 4a. Inferring from bias-dependent atomic resolution images as well as apparent height about 28 pm in average (see Supplementary Fig. 4 for details), the Fe trimer structure deduced from the DFT structural relaxations has been shown in Fig. 4b.

The zero-bias Kondo peak in the dI/dU spectrum of Fe trimer has also been resolved (topmost, 0 T curve in Fig. 4c). The magnetic-field-dependent Kondo peak splitting of Fe trimer is presented in Fig. 4c, where the comparative analyses of $\Delta(B)$ following the equivalent methodology for monomer and dimer have been arranged in Fig. 4d. The $\Delta(B)$ has been best fitted by the red line in Fig. 4d, when $S_{eff} = 3/2$, $g = 2.01 \pm 0.05$, $D = 3.06 \pm 0.48$ meV, $E = 0.22 \pm 0.05$ meV and surface parallel z-axis are extrapolated from the Eq. (1). Figure 4e summarizes the temperature-dependent dI/dU spectra (grey squares), where the thermal broadening of Kondo peak has been captured by using the Frota fits (black curves). The $\Gamma_{HWHM}(T)$ has been plotted in Fig. 4f, and the T_K value about 5.88 ± 0.48 K has been obtained by fitting to the Eq. (2). Comparing with Fe monomer and dimer, both zero-field Kondo resonance amplitude and T_K decrease all the way to the Fe trimer on stanene/Cu(111). Note that projected density of states (PDOS) of Fe atom assembly/stanene/Cu(111) have been calculated (see Supplementary Fig. 8 for details) and there is no clear trend in PDOS(E_F) related to the decrease of T_K from Fe monomer to trimer.

Evolution of Kondo temperature and Kondo resonance

Inspecting from the consistently decreased T_K values and the successive attenuation of zero-field Kondo resonance summarized in Fig. 5a, one would expect the mutual interplay between Kondo effect and magnetic interaction, especially when individual Fe dopants are self-assembled in a close proximity. The magnitude of Fe-Fe coupling in terms of dipolar, exchange and RKKY interactions[42–44] has been estimated (see Supplementary Note for details). Since dipole-dipole interaction decreases as the inverse cube of Fe-Fe interatomic distance and exchange interaction vanishes from a lack of direct 3d orbital hybridization between Sn-separated Fe atoms (see Supplementary Fig. 9 for details), the RKKY interaction turns out to be a relatively favorable mechanism.

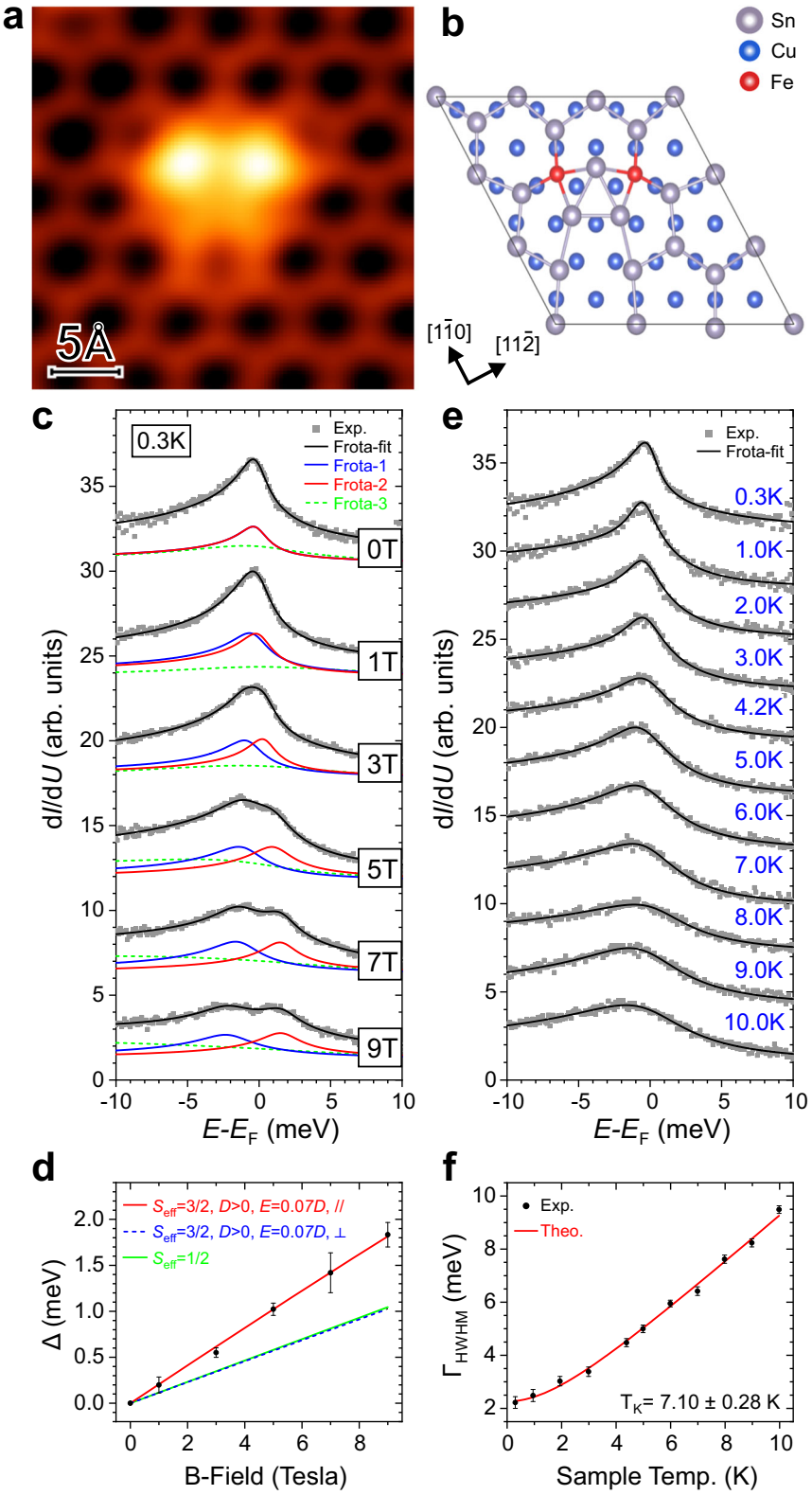

Fig. 3 | Field-dependent Kondo resonance and Kondo temperature measured from Fe dimer. **a** Atomically resolved STM topography of Fe dimer on the honeycomb-structured stanene/Cu(111). **b** Atomic Fe dimer structure fully relaxed from DFT calculations. **c** Magnetic field-dependent dI/dU spectra measured on the Fe dimer from 0 to 9 T fitted by the superposition of Frota functions. All spectra are vertically shifted for clear visibility. **d** Zeeman splittings of Kondo resonance fitted by effective spin Hamiltonian with magnetic anisotropy terms involved. **e** Temperature-dependent evolution of Kondo resonance from 0.3 to 10 K and corresponding Frota fits. **f** HWHM of Kondo resonance extracted from the Frota fits of (**e**) and $T_K = 7.10$ K can be determined by using Eq. (2). Error bars are defined by the standard deviation of fitting analyses. (stabilization parameters: $U_b = +10$ mV, $I_t = 1.0$ nA for all dI/dU curves).

Hence, we have modeled the host conduction electrons as free electron gas with Fermi wave vector k_F and the Fe atoms as magnetic impurities with quantum wells separated by a distance R. The RKKY interaction in one, two, and three-dimensional systems can be formulated by the following Hamiltonian[45]:

$$H_{\mathrm{RKKY}} = -\sum_{\mathbf{R},\mathbf{R}'} J_d^{\mathrm{RKKY}}(|\mathbf{R}-\mathbf{R}'|)\,\vec{\mathbf{S}}(\mathbf{R})\cdot\vec{\mathbf{S}}(\mathbf{R}'), \tag{3}$$

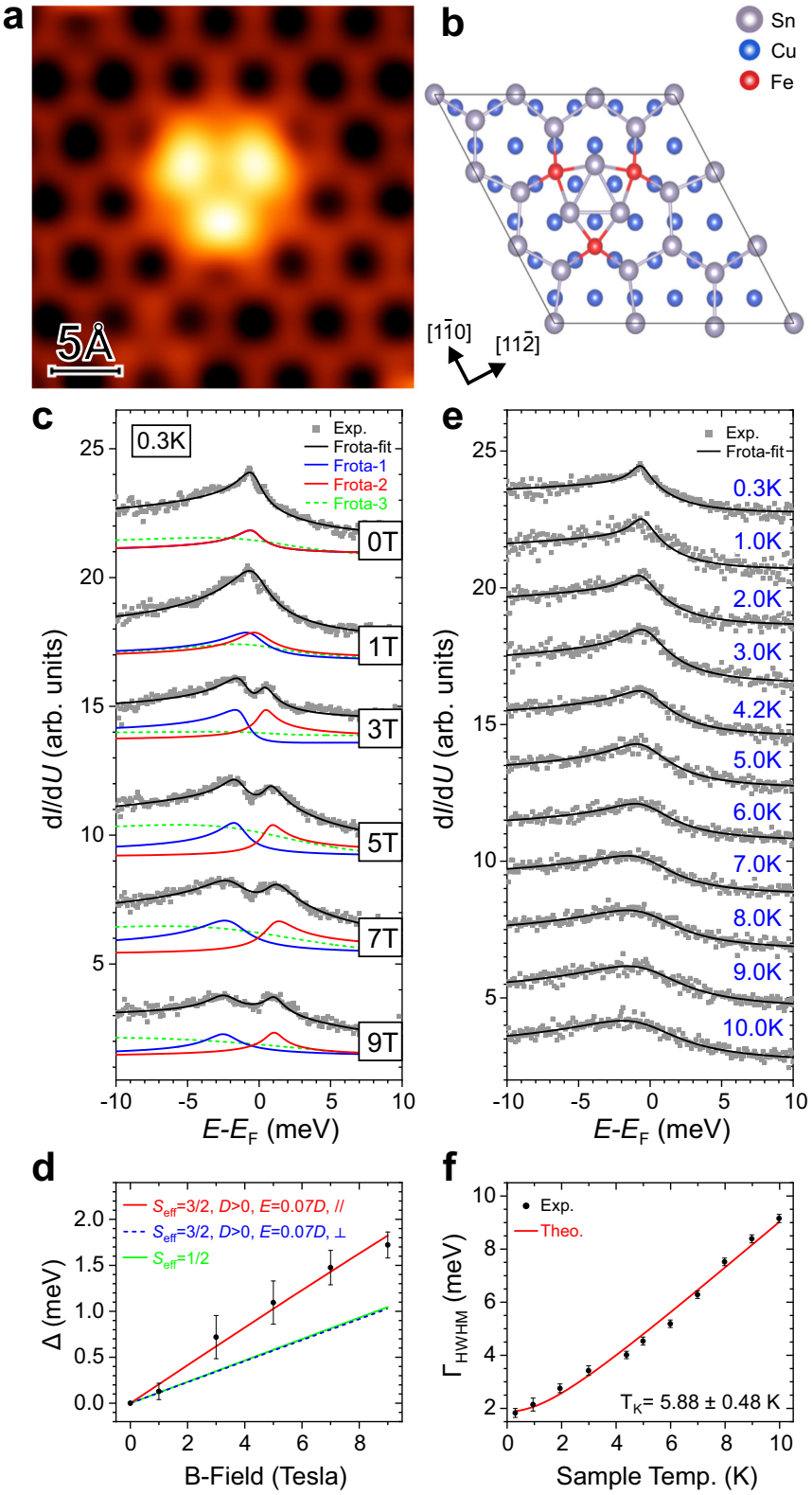

Fig. 4 | Field-dependent Kondo resonance and Kondo temperature measured from Fe trimer. **a** Atomically resolved STM topography of Fe trimer on the honeycomb-structured stanene/Cu(111). **b** Atomic Fe trimer structure fully relaxed from DFT calculations. **c** Magnetic field-dependent dI/dU spectra measured on the Fe trimer from 0 to 9 T fitted by the superposition of Frota functions. All spectra are vertically shifted for clear visibility. **d** Zeeman splittings of Kondo resonance fitted by effective spin Hamiltonian with magnetic anisotropy terms involved. **e** Temperature-dependent evolution of Kondo resonance from 0.3 to 10 K and corresponding Frota fits. **f** HWHM of Kondo resonance extracted from the Frota fits of (**e**) and $T_K = 5.88$ K can be determined by using Eq. (2). Error bars are defined by the standard deviation of fitting analyses. (stabilization parameters: $U_b = +10$ mV, $I_t = 1.0$ nA for all dI/dU curves).

$$J_d^{\mathrm{RKKY}}(R) = \pi E_F N_F^2 J_K^2 F_d(2k_F R) \quad (4)$$

where a subscript d is a spatial dimension, E_F is a Fermi energy, N_F is a density of states at the fermi energy and J_K is a Kondo coupling constant. The functions $F_d(2k_F R)$ for $d = 1, 2, 3$ are given by

$$F_1(2k_F R) = \frac{\pi}{2} - \int_0^{2k_F R} \mathrm{d}y \frac{\sin y}{y}, \quad (5a)$$

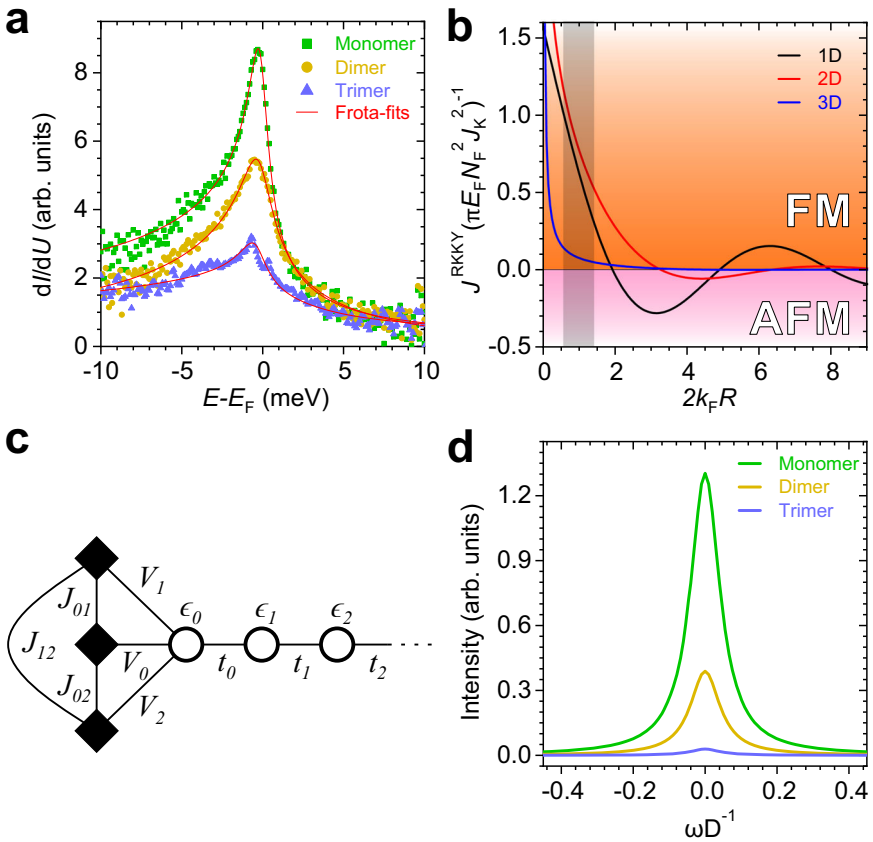

Fig. 5 | NRG analyses of RKKY-mediated Kondo resonance on Fe atom assembly. a Zero-field conductance spectra measured over the Fe impurities in monomer, dimer, and trimer structures. **b** The RKKY interaction between two magnetic impurities as a function of $2k_FR$, where, k_F is the Fermi wave vector for stanene/Cu(111) and R is the distance between impurities showing an oscillating behavior between FM and AFM for different dimensionality. The grey shaded area shows the range covering $R = 5.1$ Å and k_F from 0.05 to 0.14 Å^{-1} for the Fe atomic dopants on stanene/Cu(111). **c** The configuration of the three-impurity Kondo model mapped on a semi-infinite chain. **d** The intensity of spectral density of the zeroth impurity in the three-impurity Kondo model as a function of energy ω normalized by the bandwidth of the conduction band D (see Experimental and Theoretical Methods).

$$F_2(2k_FR) = -J_0(k_FR)N_0(k_FR) - J_1(k_FR)N_1(k_FR), \tag{5b}$$

$$F_3(2k_FR) = \left[-2k_FR\cos(2k_FR) + \sin(2k_FR)\right]/(4(2k_FR)^4). \tag{5c}$$

$J_n(x)$ and $N_n(x)$ in the $F_2(2k_FR)$ are the Bessel functions of the first and second kinds. Using the distance between Fe atoms ($R \approx 5.1$ Å) determined experimentally and the Fermi wave vector ($k_F \approx 0.05$ Å^{-1}) derived from the DFT calculation (see Supplementary Fig. 10 for details), we are able to plot the $J_d^{\mathrm{RKKY}}/(\pi E_F N_F^2 J_K^2)$ as a function of $2k_FR$ for all considered dimensions and have found that the sign of J_{RKKY} remains positive for one, two and three-dimensional systems as grey shaded region in Fig. 5b, highlighting the ferromagnetic (FM) RKKY coupling. Therefore, the RKKY interaction between the Sn-separated Fe atoms becomes substantial not only in the competition with Kondo physics, but also in the appearance of magnetic phase transition. Furthermore, we would like to denote that the theoretically deduced Kondo temperatures of dimer and trimer with respect to monomer are quantitatively comparable to experimental values, underlining the importance of RKKY-mediated Kondo effect[46–48] (see Supplementary Note).

The amplitude of Kondo peak declining from Fe monomer to trimer has also been investigated by considering the RKKY interaction in numerical renormalization group (NRG) method. The Kondo impurity model[1,40,49] in principle involves three Hamiltonian terms, i.e., $H = H_{\mathrm{imp}} + H_{\mathrm{con}} + H_{\mathrm{hyb}}$, where H_{imp} is the Kondo impurity, H_{con} is the conduction electrons, and H_{hyb} describes the interaction between the Kondo impurity and the conduction electrons. Following the standard NRG formalism[40,50–52] and consider magnetic impurities that couple to a semi-infinite chain as the schematic drawing shown in Fig. 5c, the Hamiltonian becomes:

$$H = H_{\mathrm{imp}} + \sum_{n=0}^{\infty}\sum_{\sigma=\uparrow,\downarrow}(\epsilon_n c_{n\sigma}^{\dagger}c_{n\sigma} + t_n(c_{n\sigma}^{\dagger}c_{n+1\sigma} + c_{n+1\sigma}^{\dagger}c_{n\sigma})) + \sum_{\alpha,k,\sigma} V_{\alpha k}(f_{\alpha\sigma}^{\dagger}c_{k\sigma} + \mathrm{h.c.}), \tag{6}$$

with

$$H_{\mathrm{imp}} = \sum_{\sigma=\uparrow,\downarrow}\sum_{\alpha=0,1,2}\epsilon_{f_\alpha}f_{\alpha\sigma}^{\dagger}f_{\alpha\sigma} + Uf_{\alpha\uparrow}^{\dagger}f_{\alpha\uparrow}f_{\alpha\downarrow}^{\dagger}f_{\alpha\downarrow} + \frac{1}{2}\sum_{\alpha,\beta=0,1,2}J_{\alpha\beta}(\vec{\mathbf{S}}_{\alpha}\cdot\vec{\mathbf{S}}_{\beta}). \tag{7}$$

Here $c_{n\sigma}^{(\dagger)}$ is the fermionic operator of conduction electrons with energy ϵ_n, while $f_{\alpha\sigma}^{(\dagger)}$ is the fermionic operator of $f_{\alpha\sigma}$ electrons with onsite energy ϵ_f at the α's impurity. U is the Hubbard interaction of the Kondo impurities, $V_{\alpha k}$ is the hybridization strength between the $f_{\alpha\sigma}$ electrons of the α's impurity and the conduction electrons, the exchange couplings between impurities are $J_{\alpha\beta} = J_{\beta\alpha}$, and $[\vec{\mathbf{S}}_{\alpha}]_{ij} = \frac{1}{2}f_{\alpha i}^{\dagger}[\vec{\sigma}]_{ij}f_{\alpha j}^{\dagger}$. The hybridizations $V_{\alpha k}$ can induce the RKKY interaction between impurities on top of exchange couplings $J_{\alpha\beta}$, and non-zero hybridization V_{0k} as well as the $J_{\alpha\beta}$ are considered. For simplicity, we assume the constant DOS of conduction electrons within the interval $[-1, 1]$, the constant hybridization V, $\epsilon_n = 0$, and

$$t_n = \frac{(1+\Lambda^{-1})(1-\Lambda^{-n-1})}{2\sqrt{1-\Lambda^{-2n-1}}\sqrt{1-\Lambda^{-2n-3}}}\Lambda^{-n/2}. \tag{8}$$

The crucial benefit of adopting the semi-infinite chain scheme is that Hamiltonian can be solved numerically via the iteration calculation. By using this NRG method, the Kondo resonance peak can therefore be

computed from the impurity spectral function, which is defined for $T = 0$ K as

$$A(\omega) = \frac{1}{Z_0}\sum_{\sigma,\alpha} |\langle \alpha\sigma | f_\sigma^\dagger | 0\sigma\rangle|^2 \delta(\omega + (E_\alpha - E_0)) + |\langle 0\sigma | f_\sigma | \alpha\sigma\rangle|^2 \delta(\omega - (E_\alpha - E_0)), \quad (9)$$

where Z_0 is the partition function at $T = 0$ K, and $|\alpha\sigma\rangle$ is the corresponding state with energy E_α in the Kondo impurity model mapped on the semi-infinite chain. As the spectra plotted in Fig. 5d, the intensity of Kondo resonance successively attenuates from Fe monomer to trimer, which not only reflects the essential role of RKKY interaction, but also illustrates the consistency with the experimental results in Fig. 5a. We would like to denote that our results are in agreement with the physical picture of Doniach theory, where the Kondo singlet formation can be suppressed by the RKKY interaction in multi-impurity Kondo systems[48,53,54]. Despite the Kondo effect from RKKY-coupled magnetic atoms already found in distinct systems, such as Co dimers/Cu(100)[55], Co atomic chains/Ag(111)[56], Co dimers/Cu_2N/Cu(100)[57], Mn dimers/MoS_2/Au(111)[58] and FePc molecules/Au(111)[59] etc. it remains unprecedented on the magnetic Fe atom assembly doped in the monolayer stanene/Cu(111), where the atomic spin state, magnetic anisotropy, evolution of Kondo temperature and Kondo resonance have been analyzed in detail. Additionally, for an interesting comparison, the topological band structures of stanene monolayer with/without magnetic Fe dopants have been provided in the Fig. 11 of Supplementary, where the spin-split band features might trigger feasible and associated experiments, for examples, photoemission spectroscopy, quantum transport and magnetometry measurements etc.

In summary, we have combined experiment and theory to systematically study the Kondo effect from magnetic Fe atoms self-assembled on stanene/Cu(111). According to atomic resolution STM images and self-consistent DFT structural relaxations, Fe monomer, dimer and trimer from substituting Sn atoms have been successfully synthesized on the monolayer stanene/Cu(111) at 80 K. By employing tunneling spectroscopy with high spatial and energy resolution, not only zero-bias Kondo resonance, but also magnetic-field-dependent Zeeman splitting has been resolved, where an effective spin $S_{\rm eff} = 3/2$ with $D > 0$ and $E \approx 0$ for an easy-plane magnetic anisotropy has been deduced from the effective spin Hamiltonian. In addition, a continuous reduction of Kondo temperature, i.e., from $T_{\rm K}^{\rm monomer} = 7.70 \pm 0.23$ K to $T_{\rm K}^{\rm trimer} = 5.88 \pm 0.48$ K, has been revealed from the temperature-dependent evolution of Kondo resonance, which can be explained by the indirect RKKY interaction between Sn-separated Fe atoms. Furthermore, the successive attenuation of Kondo peak amplitude from Fe monomer to trimer has been numerically simulated by using the NRG method with dominant RKKY coupling in the Kondo impurity model. From the atomic-scale magnetic doping realized by unraveling the RKKY-mediated Kondo physics, our results open a pathway toward tuning non-trivial properties of topological bands and stabilizing RKKY-coupled magnetic moments for emergent magnetic ordering in the atomically Fe-doped stanene with only one-atomic-layer thickness.

Methods

Sample preparation

The experiment was performed in the ultra-high vacuum (UHV) environment of $p \le 2.0 \times 10^{-10}$ mbar. Clean Cu(111) surface was prepared by several cycles of Ar^+ ion sputtering with an ion energy of 0.5 keV at room temperature, and followed by the thermal annealing to 1000 K afterward. To grow the flat stanene on Cu(111), the substrate was first cooled down to 80 K, and then high-purity granular Sn (99.999%, Goodfellow) was evaporated from a pyrolytic boron nitride (PBN) crucible heated in an e-beam evaporator. Subsequently, Fe atoms were deposited onto the stanene by heating a high-purity Fe-rod (99.999%, Goodfellow) in an e-beam heater while keeping the substrate at the same temperature of 80 K. Afterward, the sample was in-situ transferred to STM immediately for the measurements.

STM/STS measurement

A custom-designed low-temperature STM (Unisoku Co. Ltd.) with the base temperature of 300 mK equipped with an out-of-plane superconducting magnet of 9 T was employed to investigate the sample. All STM images were scanned in the constant-current mode with bias voltage U applied to the sample. For scanning tunneling spectroscopy (STS) measurements, a small bias voltage modulation was added to U (frequency $\nu = 2671$ Hz), such that tunneling differential conductance dI/dU spectra can be acquired by detecting the first harmonic signal by means of a lock-in amplifier.

Density function theory (DFT)

First-principles calculations based on density functional theory (DFT) were performed using the Vienna Ab Initio Simulation Package (VASP)[60–62]. The generalized gradient approximation (GGA) in the Perdew-Burke-Ernzerhof (PBE)[63] form was used for the exchange-correlation potentials with the projector augmented wave (PAW) pseudopotential[64]. The crystal structure models of Fe monomer-, dimer- and trimer-substituted stanene on Cu(111) were referred from the previous studies[16,32] with the Co atoms replaced by Fe. The lattice structures were geometrically optimized until the total energy and residual atomic forces were converged to 10^{-4} eV and -0.005 eV $\cdot$ Å^{-1}, respectively. A vacuum layer with thickness of 25 Å well-separating slabs and plane wave basis with cutoff-energy of 400 eV were chosen in the slab model calculations. The spin-orbit coupling (SOC) was included in the self-consistent-field calculations for the relaxed Fe/Sn/Cu(111) lattice models using $6 \times 6 \times 1$ Monkhorst-Pack k-grid mesh. As for bare stanene on Cu(111), higher density k-grid mesh of $24 \times 24 \times 1$ was used for the smaller unit cell. The hoping constants were calculated using the WANNIER90 code[65] based on the DFT results. The 2D Fermi surface was calculated using WannierTools[66] software package based on Wannier Hamiltonian.

Numerical renormalization group calculation

The NRG method requires three steps. The first step is to discretize the density of states (DOS) of conduction electrons using a parameter Λ, which defines the energy intervals $[\Lambda^{-n}, \Lambda^{n+1}]$ of conduction electrons coupled to the Kondo impurity. The second step is to approximate the conduction electrons in each energy interval by a single state. The last step is to map the above systems to a semi-infinite chain, in which the Kondo impurities couple to the first conduction electron by hybridization strength $V_{\alpha=0,1,2}$, and the rest of conduction electrons can be described by the tight-binding model with onsite energy ϵ_n and hopping parameter t_n. We have obtained $(J_{01}, J_{02}, \Lambda) = (0, 0, 3)$ for the monomer case, $(J_{01}, J_{02}, \Lambda) = (-0.5 * 10^{-3}, 0, 2.4)$ and $(J_{01}, J_{02}, \Lambda) = (-0.25 * 10^{-3}, -0.25 * 10^{-3}, 2.09)$ for the dimer and trimer cases, respectively. And the rest parameter $U = 10^{-3}$, $\epsilon_f = -0.5 * 10^{-3}$, $V_0 = 0.004$, and $V_1 = V_2 = J_{12} = 0$ for the spectra plotted in Fig. 5d.

Data availability

The datasets generated during and/or analyzed during the current study are available from the corresponding author on reasonable request.

Received: 28 November 2023; Accepted: 3 April 2024;
Published online: 12 April 2024

References

1. Kondo, J. Resistance minimum in dilute magnetic alloys. *Prog. Theor. Phys.* **32**, 37–49 (1964).
2. Kouwenhoven, L. & Glazman, L. Revival of the kondo effect. *Phys. World* **14**, 33 (2001).
3. Ternes, M., Heinrich, A. J. & Schneider, W.-D. Spectroscopic manifestations of the kondo effect on single adatoms. *J. Phys. Condens. Matter* **21**, 053001 (2008).
4. Li, J., Schneider, W.-D., Berndt, R. & Delley, B. Kondo scattering observed at a single magnetic impurity. *Phys. Rev. Lett.* **80**, 2893 (1998).

5. Madhavan, V., Chen, W., Jamneala, T., Crommie, M. & Wingreen, N. Tunneling into a single magnetic atom: spectroscopic evidence of the kondo resonance. *Science* **280**, 567–569 (1998).
6. Hewson, A. C. *The Kondo problem to heavy fermions*. 2 (Cambridge University Press, 1997).
7. Prüser, H., Wenderoth, M., Weismann, A. & Ulbrich, R. G. Mapping itinerant electrons around kondo impurities. *Phys. Rev. Lett.* **108**, 166604 (2012).
8. Ren, J. et al. Kondo effect of cobalt adatoms on a graphene monolayer controlled by substrate-induced ripples. *Nano Lett.* **14**, 4011–4015 (2014).
9. Prüser, H. et al. Long-range kondo signature of a single magnetic impurity. *Nat. Phys.* **7**, 203–206 (2011).
10. Schneider, L. et al. Magnetism and in-gap states of 3d transition metal atoms on superconducting re. *npj Quant. Mater.* **4**, 1–8 (2019).
11. Zhang, Y.-h et al. Temperature and magnetic field dependence of a Kondo system in the weak coupling regime. *Nat. Commun.* **4**, 1–6 (2013).
12. Otte, A. F. et al. The role of magnetic anisotropy in the Kondo effect. *Nat. Phys.* **4**, 847–850 (2008).
13. Liu, L. et al. Revealing the atomic site-dependent g factor within a single magnetic molecule via the extended kondo effect. *Phys. Rev. Lett.* **114**, 126601 (2015).
14. Nagaoka, K., Jamneala, T., Grobis, M. & Crommie, M. Temperature dependence of a single kondo impurity. *Phys. Rev. Lett.* **88**, 077205 (2002).
15. Garnier, L. et al. The kondo effect of a molecular tip as a magnetic sensor. *Nano Lett.* **20**, 8193–8199 (2020).
16. Deng, J. et al. Epitaxial growth of ultraflat stanene with topological band inversion. *Nat. Mater.* **17**, 1081–1086 (2018).
17. Zheng, X., Zhang, J.-F., Tong, B. & Du, R.-R. Epitaxial growth and electronic properties of few-layer stanene on insb (1 1 1). *2D Mater.* **7**, 011001 (2020).
18. Zhu, F.-f et al. Epitaxial growth of two-dimensional stanene. *Nat. Mater.* **14**, 1020–1025 (2015).
19. Xu, Y. et al. Large-gap quantum spin hall insulators in tin films. *Phys. Rev. Lett.* **111**, 136804 (2013).
20. Wu, S.-C., Shan, G. & Yan, B. Prediction of near-room-temperature quantum anomalous hall effect on honeycomb materials. *Phys. Rev. Lett.* **113**, 256401 (2014).
21. Zhang, G.-F., Li, Y. & Wu, C. Honeycomb lattice with multiorbital structure: Topological and quantum anomalous hall insulators with large gaps. *Phys. Rev. B* **90**, 075114 (2014).
22. Zhang, H., Wang, Z. & Xu, X. Room temperature quantum spin hall insulator: Functionalized stanene on layered pbi2 substrate. *Appl. Phys. Lett.* **111**, 072105 (2017).
23. Tokura, Y., Yasuda, K. & Tsukazaki, A. Magnetic topological insulators. *Nat. Rev. Phys.* **1**, 126–143 (2019).
24. Liu, C.-X., Zhang, S.-C. & Qi, X.-L. The quantum anomalous hall effect: theory and experiment. *Annu. Rev. Condens. Matter Phys.* **7**, 301–321 (2016).
25. Liu, C.-X., Qi, X.-L., Dai, X., Fang, Z. & Zhang, S.-C. Quantum anomalous hall effect in $Hg_{1-y}Mn_yTe$ quantum wells. *Phys. Rev. Lett.* **101**, 146802 (2008).
26. Yu, R. et al. Quantized anomalous hall effect in magnetic topological insulators. *Science* **329**, 61–64 (2010).
27. Chang, C.-Z. et al. Experimental observation of the quantum anomalous hall effect in a magnetic topological insulator. *Science* **340**, 167–170 (2013).
28. Zhang, S. et al. Giant dzyaloshinskii-moriya interaction, strong xxz-type biquadratic coupling, and bimeronic excitations in the two-dimensional crmni6 magnet. *npj Quant. Mats.* **8**, 38 (2023).
29. Chau, T. K., Hong, S. J., Kang, H. & Suh, D. Two-dimensional ferromagnetism detected by proximity-coupled quantum hall effect of graphene. *npj Quant. Mats.* **7**, 27 (2022).
30. Xiao, R.-C., Shao, D.-F., Li, Y.-H. & Jiang, H. Spin photogalvanic effect in two-dimensional collinear antiferromagnets. *npj Quant. Mats.* **6**, 35 (2021).
31. Haldane, F. D. M. Model for a quantum hall effect without landau levels: Condensed-matter realization of the “parity anomaly". *Phys. Rev. Lett.* **61**, 2015 (1988).
32. Kumar, N. et al. Self-assembly of magnetic co atoms on stanene. *Phys. Rev. Mater.* **6**, 066001 (2022).
33. Frota, H. Shape of the kondo resonance. *Phys. Rev. B* **45**, 1096 (1992).
34. Frota, H. & Oliveira, L. Photoemission spectroscopy for the spin-degenerate anderson model. *Phys. Rev. B* **33**, 7871 (1986).
35. Rosch, A., Paaske, J., Kroha, J. & Wölfle, P. Nonequilibrium transport through a kondo dot in a magnetic field: Perturbation theory and poor man’s scaling. *Phys. Rev. Lett.* **90**, 076804 (2003).
36. Gatteschi, D., Sessoli, R. & Villain, J. *Molecular nanomagnets*, vol. 5 (Oxford University Press, 2006).
37. Dubout, Q. et al. Controlling the spin of co atoms on pt (111) by hydrogen adsorption. *Phys. Rev. Lett.* **114**, 106807 (2015).
38. Žitko, R., Peters, R. & Pruschke, T. Splitting of the Kondo resonance in anisotropic magnetic impurities on surfaces. *N. J. Phys.* **11**, 053003 (2009).
39. Ternes, M. Probing magnetic excitations and correlations in single and coupled spin systems with scanning tunneling spectroscopy. *Prog. Surf. Sci.* **92**, 83–115 (2017).
40. Wilson, K. G. The renormalization group: Critical phenomena and the Kondo problem. *Rev. Mod. Phys.* **47**, 773 (1975).
41. Žitko, R. & Pruschke, T. Energy resolution and discretization artifacts in the numerical renormalization group. *Phys. Rev. B* **79**, 085106 (2009).
42. Ruderman, M. A. & Kittel, C. Indirect exchange coupling of nuclear magnetic moments by conduction electrons. *Phys. Rev.* **96**, 99 (1954).
43. Kasuya, T. A theory of metallic ferro-and antiferromagnetism on Zener’s model. *Prog. Theor. Phys.* **16**, 45–57 (1956).
44. Yosida, K. Magnetic properties of cu-mn alloys. *Phys. Rev.* **106**, 893 (1957).
45. Tamura, H., Shiraishi, K. & Takayanagi, H. Tunable exchange interaction in quantum dot devices. *Jpn J. Appl. Phys.* **43**, L691 (2004).
46. Nejati, A. & Kroha, J. Oscillation and suppression of kondo temperature by rkky coupling in two-site kondo systems. *J. Phys. Conf. Ser.* **807**, 082004 (2017).
47. Bork, J. et al. A tunable two-impurity kondo system in an atomic point contact. *Nat. Phys.* **7**, 901–906 (2011).
48. Nejati, A., Ballmann, K. & Kroha, J. Kondo destruction in rkky-coupled kondo lattice and multi-impurity systems. *Phys. Rev. Lett.* **118**, 117204 (2017).
49. Anderson, P. W. A poor man’s derivation of scaling laws for the kondo problem. *J. Phys. C: Solid State* **3**, 2436 (1970).
50. Jones, B. A. & Varma, C. M. Study of two magnetic impurities in a fermi gas. *Phys. Rev. Lett.* **58**, 843–846 (1987).
51. Bulla, R., Costi, T. A. & Pruschke, T. Numerical renormalization group method for quantum impurity systems. *Rev. Mod. Phys.* **80**, 395 (2008).
52. Žitko, R. & Bon ča, J. Numerical renormalization group study of two-channel three-impurity triangular clusters. *Phys. Rev. B* **77**, 245112 (2008).
53. Doniach, S. The kondo lattice and weak antiferromagnetism. *Phys. B +C.* **91**, 231–234 (1977).
54. Paschen, S. & Si, Q. Quantum phases driven by strong correlations. *Nat. Rev. Phys.* **3**, 9–26 (2020).
55. Wahl, P. et al. Exchange interaction between single magnetic adatoms. *Phys. Rev. Lett.* **98**, 056601 (2007).
56. Moro-Lagares, M. et al. Real space manifestations of coherent screening in atomic scale kondo lattices. *Nat. Commun.* **10**, 2211 (2019).

57. Spinelli, A. et al. Exploring the phase diagram of the two-impurity kondo problem. *Nat. Commun.* **6**, 10046 (2015).
58. Trishin, S. et al. Tuning a two-impurity kondo system by a moiré superstructure. *Phys. Rev. Lett.* **130**, 176201 (2023).
59. Tsukahara, N. et al. Evolution of kondo resonance from a single impurity molecule to the two-dimensional lattice. *Phys. Rev. Lett.* **106**, 187201 (2011).
60. Kresse, G. & Hafner, J. Ab initio molecular dynamics for liquid metals. *Phys. Rev. B* **47**, 558 (1993).
61. Kresse, G. & Furthmüller, J. Efficiency of ab-initio total energy calculations for metals and semiconductors using a plane-wave basis set. *Comp. Mater. Sci.* **6**, 15–50 (1996).
62. Kresse, G. & Furthmüller, J. Efficient iterative schemes for ab initio total-energy calculations using a plane-wave basis set. *Phys. Rev. B* **54**, 11169 (1996).
63. Perdew, J. P., Burke, K. & Ernzerhof, M. Generalized gradient approximation made simple. *Phys. Rev. Lett.* **77**, 3865–3868 (1996).
64. Kresse, G. & Joubert, D. From ultrasoft pseudopotentials to the projector augmented-wave method. *Phys. Rev. B* **59**, 1758 (1999).
65. Pizzi, G. et al. Wannier90 as a community code: new features and applications. *J. Phys. Condens. Matter* **32**, 165902 (2020).
66. Wu, Q., Zhang, S., Song, H.-F., Troyer, M. & Soluyanov, A. A. Wanniertools: An open-source software package for novel topological materials. *Comput. Phys. Commun.* **224**, 405–416 (2018).

Acknowledgements

P.J.H. acknowledges support from C.L.H. for helium liquefier system operation in the instrumentation center of National Tsing Hua University under Grants No. MOST-110-2731-M-007-396-001 and MOST-111-2731-M-007-001, National Science and Technology Council of Taiwan under Grant Nos. NSTC-112-2636-M-007-006 and NSTC-112-2112-M-007-037, Ministry of Science and Technology of Taiwan under Grants No. MOST-111-2636-M-007-007 and MOST-110-2636-M-007-006, and center for quantum technology from the featured areas research center program within the framework of the higher education sprout project by the Ministry of Education (MOE) in Taiwan. P.-Y.C. acknowledges support from National Science and Technology Council of Taiwan under Grant No. NSTC-112-2636-M-007-007. H.-T.J. acknowledges support from National Science and Technology Council of Taiwan under Grant No. NSTC 112-2112-M-007 -034 -MY3, and also from the NCTS, NCHC, CINC-NTU and AS-iMATE-113-12 in Taiwan.

Author contributions

N.K., Y.H.L. and I.J. contributed equally to this work. N.K., Y.H.L., C.J.C., T.H.L. and P.J.H. carried out the STM/STS experiments and analyzed the data. Y.S.L. and H.T.J. performed the DFT calculations. I. J. and P.Y.C. performed the NRG simulations. H.T.J., P.Y.C. and P.J.H. coordinated and supervised the project. All authors discussed the results and contributed to the paper.

Competing interests

The authors declare no competing interests.

Additional information

Supplementary information The online version contains supplementary material available at https://doi.org/10.1038/s41535-024-00647-1.

Correspondence and requests for materials should be addressed to Horng-Tay Jeng, Po-Yao Chang or Pin-Jui Hsu.